Structure of low-lying states of ^{10,11}C from proton elastic and inelastic scattering

C. Jouanne, V. Lapoux,* F. Auger, N. Alamanos, A. Drouart, A. Gillibert,
G. Lobo,† A. Musumarra,‡ L. Nalpas, E. Pollacco, J-L. Sida, and M.Trotta§
CEA-SACLAY DSM/DAPNIA/SPhN F-91191 Gif-sur-Yvette, France.

Y. Blumenfeld, E. Khan, T. Suomijärvi, T. Zerguerras
Institut de Physique Nucléaire, IN_2P_3-CNRS, F- 91406 Orsay, France

P. Roussel-Chomaz, H. Savajols
GANIL, Bld Henri Becquerel, BP 5027, 14021 Caen Cedex, France

A. Lagoyannis, A. Pakou
Department of Physics, The University of Ioannina, 45110 Ioannina, Greece Chmpn.

(Dated: May 12, 2005)

Abstract

To probe the ground state and transition densities, elastic and inelastic scattering on a proton target were measured in inverse kinematics for the unstable ^{10}C and ^{11}C nuclei at 45.3 and 40.6 MeV/nucleon, respectively. The detection of the recoil proton was performed by the MUST telescope array, in coincidence with a wall of scintillators for the quasi-projectile. The differential cross sections for elastic and inelastic scattering to the first excited states are compared to the optical model calculations performed within the framework of the microscopic nucleon-nucleus Jeukenne-Lejeune-Mahaux potential. Elastic scattering is sensitive to the matter root mean square radius found to be 2.42 $\pm$0.1 fm and 2.33 $\pm$0.1 fm, for ^{10,11}C, respectively. The transition densities from cluster and mean-field models are tested and the cluster model predicts the correct order of magnitude of cross sections for the transitions of both isotopes. Using the Bohr-Mottelson prescription, a profile for the ^{10}C transition density from the 0^+ ground to the 2^+_1 state is deduced from the data. The corresponding neutron transition matrix element is extracted : $M_n = 5.51 \pm 1.09$ fm^2.

PACS numbers: 23.20.Js,25.40.Ep,25.60.-t,27.20.+n

*E-mail: vlapoux@cea.fr; URL: http://www-dapnia.cea.fr/Sphn/Exotiques

†permanent address :Geel

‡permanent address :INFN-Laboratori Nazionali del Sud, Via S. Sofia 44, 95123 Catania, Italy

§permanent address :INFN - Sezione di Napoli, Via Cintia, 80126 Napoli, Italy

I. INTRODUCTION

For stable nuclei, proton and neutron ground state density distributions usually display similar behaviours. In a first approach, the neutron density can be considered as proportional to the proton density in the ratio N/Z. The proton density can be obtained from the charge distribution measured experimentally through electron scattering [1]. Nevertheless, it was suggested that, provided a high enough excitation energy, clustering effects could be found in the light stable nuclei. In 1968, K. Ikeda [2] built a diagram based on the mass excess of the nuclei. He suggested that clusters could be formed in a nucleus for excitation energies in the vicinity of the fragment emission thresholds. These cluster fragments were constituted by alpha particles, like in the three alpha-cluster in ^{12}C which was located at an excitation energy close to 7.27 MeV.

A renewed interest for the clustering in light nuclei has been prompted by the availability of radioactive beams far from stability. Recently a new scheme was proposed (Von Oertzen-Ikeda's rule) [3], and predictions were given for stable and radioactive nuclei. It was assumed that bound covalent molecular structures might appear in neutron-rich nuclei for an excitation energy close to the fragmentation thresholds for alpha, neutrons or other clusters. The predictions for stable nuclei are in agreement with the available experimental observations, like the formation of an alpha-chain in ^{12}C at high excitation energy [4] and the structure of ^{8}Be in two alpha-particles.

In weakly-bound nuclei, with low energy particle emission thresholds, alpha-clustering is expected to be found at lower excitation energies than for stable isotopes. The important role that alpha-clustering should play for the beryllium, boron and carbon chains is underlined in Ref. [3], based upon the results obtained within the Antisymmetrized Molecular Dynamics (AMD) [5] framework. This model was applied to neutron-rich nuclei, from lithium to carbon, and suggest important alpha-clusterization phenomena for light neutron-rich nuclei. For instance, for the carbon chain, in the framework of AMD, the shape of the neutron distribution is found to be strongly dependent on the neutron number and varies rapidly from prolate to spherical or oblate. The nuclei ^{10,11}C, like all the other carbon isotopes described in AMD theory [5] are expected to have a proton density for the ground state with an oblate deformation, and a different shape for the neutron density : prolate for ^{10}C and triaxial for ^{11}C. This is in contrast with the usual picture for stable nuclei of homothetic

shapes for proton and neutron densities.

The neutron-deficient ^{10}C and ^{11}C are short-lived nuclei, with half-lives of 19 s and 20 min. Their low-lying spectroscopy is relatively well-known [6], as shown in Fig.1, where the excited states below the proton separation threshold, S_p=4.01 MeV for ^{10}C and 8.69 MeV for ^{11}C, are shown. From interaction cross section experiments, and via Glauber-model calculations, proton and neutron rms radii were indicated for ^{10}C [7] : $r_p = 2.31 \pm 0.03$ fm and $r_n = 2.22 \pm 0.03$ fm, and for ^{11}C [8] : $r_p = 2.13 \pm 0.06$ fm and $r_n = 2.10 \pm 0.06$ fm.

The transition strength B(E2,$0^+ \rightarrow 2_1^+$) for ^{10}C is known from Doppler shift measurements, with an adopted value of 61.5 ± 10 e^2.fm^4 [9]. For ^{11}C the low-lying excited states are also known but the transition strengths from the ground to the first excited states have not been measured. In this article, the structure of ^{10,11}C is investigated through (p,p') measurements. As shown for the ^{6}He(p,p') reaction performed at 40 MeV/nucleon [10], when the measured angular range is limited to 75 deg in the center of mass (c.m.) frame ($75^\circ_{c.m.}$), the elastic scattering is rather insensitive to details of the ground state density like the presence of a halo. These features are better investigated through proton inelastic scattering which is sensitive to the shape of the density [11, 12]. Knowing the proton transition strength, it is possible to deduce the neutron transition strength from (p,p') measurements. Using this probe, with ^{10,11}C radioactive beams, we can obtain direct structure information for the ^{10,11}C nuclei (matter root mean square radius, low-lying spectroscopy).

The analysis of the inelastic scattering to the first excited states is performed within the framework of a microscopic interaction potential including theoretical neutron and proton ground state (gs) and transition densities. It allows us to test the description of these nuclei, in terms of the mean-field approach and the AMD cluster structure model, and also to deduce interesting features of the density profiles. In the case of the ^{10}C, the E2 electromagnetic (EM) transition rate B(E2) for $0^+ \rightarrow 2_1^+$ is known, and also the corresponding B(E2) value (related to the square of the proton transition matrix element M_p) for the mirror transition in ^{10}Be. Usually, following the prescription from Bernstein, Brown and Madsen [11], charge symmetry and charge independence are assumed, and the mirror symmetry is applied to obtain the neutron transition matrix element M_n from the EM decay rate of the mirror transition. In Ref. [11], this method was checked for several mirror nuclei, of masses ranging from $A = 17$ (^{17}O,F) to $A = 42$ (^{42}Ca,Ti). They showed that the M_n value for a given transition in a nucleus (obtained via a hadronic probe) could be evaluated from the proton

transition matrix M_p value, obtained for the corresponding transition in the mirror nucleus. This transition rate is measured using an EM probe.

Using radioactive beams, it is possible to check the mirror symmetry method for a wider range of isospin values, by investigating the transitions for mirror nuclei far from stability, for neutron-rich or neutron-deficient species. Recently, it was done in [13], where the mirror method was successfully checked for the $A = 32$ $T = 2$ multiplet. In contrast, the isospin symmetry breaking was suggested for the A=38 nuclei in [14] and the $A = 30$ $T = 1$ multiplet [15]. Furthermore, in the case of light exotic nuclei, for a mirror pair composed by a neutron-deficient and a neutron-rich nucleus, like ^{10}C and ^{10}Be, this symmetry may be questioned. These nuclei have a large difference between neutron and proton numbers, compared to their stable isotopes, the particle threshold energies are low, inducing stronger coupling to excited states in the continuum, and the large Coulomb effect in the case of ^{10}C (Z/N=1.5) may contribute to a significant violation of the mirror symmetry. In the present work, the M_n factor for ^{10}C will be deduced directly from the (p,p') measurement, and compared to the M_n value given by the mirror symmetry. This will allow to check the validity of the mirror assumption.

In the following, we present the experiment carried out at the GANIL facility to study the elastic and inelastic scattering to the first excited states, below the proton separation threshold, for the nuclei ^{10,11}C. In order to test the analysis procedure, elastic and inelastic scattering of ^{12}C on proton was also measured.

In Section II, the production of the beams and the experimental set-up are detailed.

In Section III, the microscopic nucleus-nucleon interaction used to analyze the elastic scattering on protons is described. It is calculated using the microscopic, complex and parameter-free JLM potential [16]. This potential is used to perform the Distorted Wave Born approximation (DWBA) calculations leading to the inelastic (p,p') cross sections. The JLM calculations are first applied to our reference case, the ^{12}C(p,p') cross sections. The theoretical ground state and transition densities of ^{10,11}C provided by the AMD model [17] and by the HF+BCS and Quasiparticle-Random Phase Approximation (QRPA) formalism are examined in Section IV. They are used to generate the microscopic JLM potential included in the (p,p') calculations.

Conclusions on the structure of the neutron-deficient radioactive carbon isotopes are given in Sec. V.

II. EXPERIMENTAL SET-UP

The elastic and inelastic differential cross sections of ^{10,11}C on a proton target were measured with the MUST [18] telescopes. MUST ("MUr à STrips", wall of strips) is an array devoted to the inverse kinematics measurements of direct reactions induced by heavy ion beams on light target (proton, deuton targets).

We detail below the beam production, the detection system including the MUST array, the plastic wall for fragment detection and two "CATS" beam tracking detectors. A sketch of the experimental device in the reaction chamber can be found in Fig.2.

A. Beam production and identification

The ^{10,11}C secondary beams were produced successively by fragmentation of a 95 A.MeV ^{12}C beam delivered by the two GANIL cyclotrons, on a 1710 mg/cm^2 (1930 mg/cm^2 for ^{11}C)-thick carbon production target located between the two superconducting solenoids of the SISSI device (Superconducting Intense Source for Secondary Ions) [19, 20].

This device is located at the exit of the second cyclotron and at the entrance of the beam analysing α-spectrometer. It allows for an improved collection and transmission of the secondary beams to the different experimental areas. A 0.2 mm thick mylar degrader was put in the Alpha-spectrometer in order to purify the secondary beam. The beam purity was checked by a 300 μm-thick Si detector located inside the chamber, using the ΔE energy loss versus Time of flight (TOF) method. The TOF was taken between a microchannel plate (mcp) detector, located at the exit of the Alpha spectrometer, and the time given by the particle detected in the Faraday plastic (Fig.2) at a distance of 64 m from the mcp.

After purification, the ^{10}C beam had no contaminant whereas the ^{11}C represented around 75% of the total secondary beam, with ^{12}C as main contaminant. The intensities of the ^{10,11}C secondary beams on the reaction target were of the order of 5. 10^5 and 5. 10^6 particles per second (pps) respectively, at an energy of 45.3 and 40.6 MeV/nucleon.

B. Beam profile

As the emittance of a radioactive beam produced by fragmentation is large, the beam spot usually covering 1 cm^2 on the target with a maximum angular divergence of 1°, two position sensitive detectors, the low pressure multi-wire trajectory chambers CATS [21] ("Chambres à Trajectoires de Saclay", Trajectory Chambers of Saclay), were used to improve the definition of the position of the incoming ion on the target. They provided the beam position and time tracking particle by particle. CATS1 and CATS2 were located at 159.2 cm and 27.5 cm upstream of the target (distances between detectors and target are given in Fig. 2). These detectors measured event by event the horizontal (H) and vertical (V) positions perpendicular to the beam axis providing the impact point and the incident angle of the particles on the target with a FWHM resolution of 1.1 mm (H), 1.2 mm (V) and 0.1°. Figure 3 presents the profiles of the ^{11}C beam at 40.6 MeV/n on the two CATS detectors and the resulting beam profile reconstructed on the proton target. The counting rate was reduced to 3. 10^5 pps for both ^{10}C and ^{11}C beams in order to use these beam tracking detectors under standard conditions. These detectors were required to obtain a good angular resolution for the scattering angle and enough excitation energy resolution to separate the excited states of ^{11}C. We will show in Sec. II E that their use is necessary to separate these states.

C. Proton detection

The experimental apparatus MUST [18], an array of eight three-stage telescopes, 6 × 6 cm^2 each, specifically designed to detect light charged particles was used to measure angular distributions for elastic and inelastic scattering of ^{10,11}C radioactive beams on proton. Using the MUST array, similar measurements were done for oxygen isotopes [22] and ^{6}He nucleus [10]. The first stage is a 300 μm-thick double-sided Si-strip detector (DSSD) which provides horizontal and vertical positions, time-of-flight with respect to a beam detector and energy loss of the recoil proton ; the second 3 mm-thick Si(Li) stage gives the proton energies up to 25.4 MeV and the third stage of 1.5 cm-thick CsI detects protons up to 75 MeV. The MUST detectors were assembled in a wall configuration which was located at 15 cm from the target, and the vertical axis of the wall was rotated by an angle of 63 deg. (63°_{lab}) with respect to the beam axis, in the laboratory (lab) frame. This position allowed to cover the

angular range between 45 and 90°_{lab}. At this distance, the 1 mm wide strips result in an angular resolution of 0.4° for the detection of the scattered particle, in the laboratory frame.

For the less energetic recoil particles which are stopped in the first Si-stage, like protons with energies below 6 MeV, the separation between p,d, triton and ^{3,4}He is operated with the energy E versus TOF technique. The particles are identified in the correlation plot constructed between their energy loss ΔE in the Si-strip detector and their TOF. This TOF is measured between the Si-stage and the start given by the passage of the incident particle in the second beam tracking detector CATS. The overall time resolution was 1.4 ns. In Fig.4 the left panel presents the E-ΔE plot, where the events for p,d and t are shown by the lines, and the right one shows the E-TOF correlation spectrum, the selection of the events for protons is shown by the contour.

For energies higher than 6 MeV the protons punch through to the 2^{nd} stage, and the identification is performed by the E-ΔE method between the energy deposited in the SiLi stage and the ΔE energy loss in the Si-stage. A typical plot is shown in Fig. 4. At 25.4 MeV the proton punches through the 3mm-thick SiLi and is detected in the CsI. In this experiment, the energy threshold for the measurement in the first Si-stage was 1 MeV. For the different sets of data, the angular range in the c.m. frame is from $10^{\circ}_{c.m.}$ to $50^{\circ}_{c.m.}$, determined by the detection of the protons from 1 MeV up to 25.4 MeV (the data presented here correspond to events for which the protons are stopped in the first two telescope stages) and for angles between 45 to 90°_{lab} in the laboratory.

D. Detection of the ejectile

In order to select the reaction channel and to eliminate background, the recoiling proton was detected in coincidence with the ejectile in the forward direction. The ejectile was detected in a plastic wall, located 75 cm behind the target and made of 6 horizontal bars of BC408, 8×50 cm^2 and 3 cm-thick. Each bar was read out by a photo-multiplier on both sides. For the most forward angles where the counting rates are very high, a small 2.8 cm-diameter plastic scintillator (referred as the Beam plastic in Fig. 2) was centered at zero degrees to collect, identify and count the beam particles. The identification of the heavy projectile in the Faraday plastic is presented in Fig.5 in the case of the ^{11}C incident beam : two spots can be seen and they correspond to the ^{11}C, and to the ^{12}C contaminant.

The coincidence with the ejectile allows to suppress the protons coming from reactions induced by the beam contaminants on the target, and also the protons emitted from excited nuclei produced in central collisions of the beam on the carbon contained in the target. Moreover, to check the background due to the carbon content in the target, a measurement on a carbon target is also carried out during the experiment as will be explained in Sec. II F.

Elastic and inelastic angular cross sections of ^{10,11}C(p,p') were measured on a 1.48 mg/cm^2 and a 8.25 mg/cm^2-thick polypropylene target $(CH_2CHCH_3)_n$ (density of 0.896 g/cm^3).

E. Kinematics and excitation energy spectra

To measure angular distributions down to $10^\circ_{c.m.}$ where the energy of the recoiling protons decreases to 1 MeV, the 1.48 mg/cm^2-thick polypropylene target was used. Good statistics at larger angles were obtained by using the 8.25 mg/cm^2-thick target. The events considered to build the kinematical spectra, and afterwards to extract the (p,p') cross sections, are those for which there is a proton in coincidence with the heavy ejectile, and a particle detected in CATS 1 and 2 providing the incident trajectory and the beam profile shown in Fig. 3. The excitation energy spectra are calculated from the kinematical properties of the scattered protons. In Fig. 6 the left spectrum presents the kinematical plot of the scattered proton obtained in the case of the reaction p(^{11}C,p') at 40.6 MeV/nucleon on the 1.48 mg/cm^2 polypropylene target : it is the correlation matrix of the proton energy E^p_{lab} versus its scattering angle θ^p_{lab}. The right panel shows its projection as the ^{11}C excitation energy E^* spectrum. This spectrum is constructed from the scattering angle given by the MUST array, without taking into account the incident angle given by the CATS detectors. The ^{11}C beam impact is considered as point-like and perpendicular to the target. The curve drawn in the matrix corresponds to the kinematical loci of the elastic scattering. Only one peak-structure at zero excitation energy appears and the other expected peaks, corresponding to the excited states of ^{11}C are not resolved.

Now, in the reconstruction of the proton scattering angle, we take into account event by event the impact point and the incident angle of the beam on the target. We present in Fig. 7 the results obtained for ^{12,11,10}C(p,p') applying this reconstruction method, the left column shows the scattering plots, and the right one the projected excitation energy spectra. The spectra obtained for ^{11}C are presented in the second line, they correspond to the same

events as those considered to construct the spectra shown in Fig. 6.

Taking into account the beam profile, it is now possible to separate clearly the different excited states in the $(\theta^p_{lab}; E^p_{lab})$ matrix and in the excitation energy E^* spectrum in Fig. 7. The full width half-maximum (FWHM) of the peak corresponding to the elastic scattering events has decreased from about 3.4 MeV (Fig. 6) to 700 keV for ^{11}C (Fig. 7).

The upper plots of Fig. 7, for slowed down primary beam ^{12}C at 36.3 MeV/nucleon and a 8.25 mg/cm^2-thick target, shows that the ground and first excited states 2^+ and 3^- are clearly identified. Their centroids are located at 20 keV, 4.46 MeV and 9.70 MeV respectively, in excellent agreement with the values tabulated in [6] : 0, 4.44 and 9.64 MeV. The 0^+ state located at 7.65 MeV is weakly excited. The FWHM of the ground state peak is 940 keV.

In the second line of Fig. 7, for ^{11}C(p,p') events on the 1.48 mg/cm^2-thick target, the calculated kinematical curves are drawn for the elastic scattering, and inelastic scattering from ground to the $1/2^-$, $5/2^-$ and $7/2^-$ states (curves from right to left). We observe the ground state $3/2^-$, the excited states $1/2^-$, $5/2^-$ and $7/2^-$ at the respective energies of 13 keV, 2.02 MeV, 4.33 MeV and 6.50 MeV. The tables (Fig.1) give the excited states at 2.00, 4.32 and 6.48 MeV respectively. Here, the ^{11}C ground state width is 680 keV (FWHM). The resolution depends on the target thickness, especially for low energy protons emitted at small c.m. angles. When the 8.25 mg/cm^2-thick target is used, the resolution is degraded to 970 keV.

The lower plots in Fig. 7 are obtained for ^{10}C(p,p') events on the 1.48 mg/cm^2 target, with selection of the ^{10}C in the plastic wall and protons in MUST. The ground state for ^{10}C is observed at 23 keV and the first state 2^+ at 3.36 MeV (adopted value 3.35 MeV). The energy resolutions of the ground state peaks are 720 and 990 keV for the 1.48 and 8.25 mg/cm^2 targets, respectively. No structure above the one-proton separation energy (8.7 MeV for ^{11}C, 4 MeV for ^{10}C) can be seen due to the imposed coincidence with ^{11}C (^{10}C) in the plastics.

These results demonstrate the importance of measuring event by event the impact point and the incident angle of the beam particles, in order to reconstruct with enough precision the scattering angle of the proton, when using beams of poor optical qualities. This reconstruction method provides the centroids of the peaks with a precision, around 20keV, which is excellent for a charge particle measurement.

F. Cross sections

The numbers of incident particles for the ^{10}C+p scattering measurements on the 1.48 and 8.25 mg/cm^2 polypropylene targets were 7.14 10^9 (^{11}C : 1.02 10^{10}) and 2.1 10^9 (^{11}C : 6.66 10^9) pps, respectively. In Fig.7, for ^{10}C (lower right panel) the background is small, we show below that a good separation between the ground and the 2^+ states can be operated.

To determine the background induced in the energy excitation spectra by the carbon content in the polypropylene target we performed a measurement with a 6 μm-thick carbon target. Due to the good selection of the ejectile and of the proton in coincidence, this background contributes for less than ± 0.5% to the global systematical error bar on the background subtraction. To evaluate the whole background subtraction in the energy excitation spectrum, we have evaluated the angular distribution of the background and of the elastic scattering for a similar range of excitation energy. From the comparison of the cross sections for various angular slices we evaluated the global error bar on the background subtraction to ± 1 %.

For all the experimental angular distributions which will be presented in the next section, the error bars given are statistical. We have estimated the overall value for the systematical error bars in the angular distributions. They come from the detection efficiency and reconstruction process, which gives ± 3 % total uncertainty (including the effect of the subtraction of the background ± 1 %), the target thickness (± 5%) and the number of incident particles (± 2%). This results in a total systematic error (± 6%) which is the main error on the normalization of the extracted elastic and inelastic differential cross sections.

The angular distributions for the proton elastic and inelastic to the 2^+ state (4.44 MeV) of ^{12}C can be seen in Fig.8. No data point is given between $24^\circ_{c.m.}$ et $30^\circ_{c.m.}$ for the elastic scattering, this is due to the energy threshold effect of 1 MeV produced by the SiLi detectors of the second stage of MUST, which results in a bad estimation of the proton energy. Consequently we do not give the cross sections corresponding to the protons in this specific region. For the scattering of ^{10}C and ^{11}C the same effect will be found.

III. NUCLEON-NUCLEUS INTERACTION POTENTIAL

A. JLM potential

The nucleon-nucleus potential used in this study is the microscopic, complex and parameter-free JLM (Jeukenne, Lejeune, Mahaux) potential [16], parameterized for incident energies up to 160 MeV. This potential is based upon infinite matter calculations, and it is built on the Reid hard-core Nucleon-Nucleon interaction, using the Brueckner-Hartree-Fock approximation.

The local complex potential $U_{JLM}(\rho, E)(r) = V(\rho, E)(r) + iW(\rho, E)(r)$ is derived in the case of a finite-size nucleus of density $\rho(r)$, (neutron and proton densities ρ_n and ρ_p) by applying the Local Density Approximation (LDA). This LDA is improved by folding the potential by a Gaussian function $\exp[-\vec{r}^2/t^2]$ to take into account the short-range of the nuclear interaction, and with t fixed to 1. fm (see in [23] for details).

The potential depends on the incident energy E and on the neutron and proton densities of the nucleus. This potential allows a good reproduction of large sets of nucleon-nucleus data [23–26]. In order to fit the nucleus-nucleon data, the JLM potential U_{JLM} may need to be slightly modified, by varying the normalization factors λ_V and λ_W for the real V and W imaginary parts :

$$U_{JLM}(\rho, E)(r) = \lambda_V V(\rho, E)(r) + i\lambda_W W(\rho, E)(r) \tag{1}$$

For A $\geq$ 20, the variations of λ_V and λ_W are usually less than 10% ; these factors are close to 1 for all A $\geq$ 20 stable nuclei. In the case of light nuclei (A $\leq$ 20), it was shown that usually $\lambda_W = 0.8$ [24]. We adopt this renormalization as the standard normalization of JLM for light nuclei.

B. (p,p') inelastic scattering

The inelastic (p,p') angular cross sections are obtained through DWBA calculations including the JLM potential. They are performed with the TAMURA code [27].

The entrance, transition and exit channel potentials are defined with the ground state and transition densities. The normalization of the real and imaginary parts is fixed with the values obtained in the analysis of the elastic scattering. For a J_i to J_f transition the

density is written : $\rho^{tr} = \langle \Psi_f | \delta(\overrightarrow{r} - \overrightarrow{r'}) | \Psi_i \rangle$. The calculated inelastic (p,p') cross sections are sensitive to the M_n and M_p factors, which are the radial moments of the transition densities, defined as :

$$M_{p,n} = \int r^{l+2} \rho^{tr}_{p,n} dr \tag{2}$$

where l is the multipolarity of the transition. The M_p factor for a J_i to J_f transition is directly related to the corresponding B(El) transition strength value obtained by an electromagnetic experiment (Coulomb excitation, electron scattering or lifetime measurements). We adopt here the following convention for the relationship between $|M_p|$ and B(E2) :

$$B(E2, J_i \rightarrow J_f) = e^2 \frac{1}{(2J_i + 1)} |M_p|^2 \tag{3}$$

The models of elastic and inelastic scattering on proton including the JLM potential were proven to be reliable to extract the fundamental quantities such as M_n/M_p without ambiguity for the stable nuclei [23] as well as for the exotic nuclei [22, 25]. A careful analysis of the elastic scattering is required in the case of weakly-bound nuclei in order to have a correct treatment of the coupling effects, as will be explained in Sec. III D.

A simple analysis of the (p,p') can be performed using the Bohr-Mottelson prescription (also ascribed as the phenomenological Tassie form in Ref. [12]) for the densities. The proton (p) or neutron (n) transition density is then obtained by derivating the ground state density :

$$\rho^{tr,l}_{p(n)}(r) = -\alpha^l_{p(n)} r^{l-1} \frac{d\rho_{p(n)}}{dr} \tag{4}$$

The proton density is normalized with the α^l_p by requiring that its moment $|M_p|$ should satisfy Eq. 3 with B(E2) obtained by electromagnetic measurements. $|M_n|$ is then deduced by adjusting the calculated (p,p') cross sections on the data.

C. ^{12}C(p,p') as a test reaction

During the same experiment, the proton elastic and inelastic scattering from ^{12}C were measured in inverse kinematics, using a ^{12}C degraded beam produced at 36.3 MeV/nucleon. The experimental conditions (beam line, settings of the telescope array) were the same as for ^{10,11}C data taking. Since other ^{12}C(p,p') measurements at various energies are available in the literature, this measurement provides a reference to cross-check the experimental setup,

the efficiency of our detection system, the reconstruction procedure and the background subtraction. It can be compared to the previous data, measured from 31 to 46 MeV/nucleon in direct kinematics. Moreover, since ^{12}C is a stable N=Z nucleus for which the densities were measured, a JLM calculation can be done using these densities and compared to the set of ^{12}C data.

The ground state proton density of ^{12}C is parameterized as a two-parameter Fermi (2pF) function :

$$\rho = \rho_o \frac{1}{1 + exp\{(r - R_o)/a\}} \tag{5}$$

with the radius $R_o = 2.1545$ fm, diffuseness $a = 0.425$ fm and $\rho_o = 0.207$ fm^{-3}. These parameters were adjusted in Ref. [28] to reproduce closely the charge rms radius [29] deduced from elastic electron scattering measurements, and the diffuseness of the matter density distributions obtained from shell model calculations [28]. The rms radius is of 2.3 fm, close the empirical rms radius of the proton distribution (2.33 ± 0.01 fm) obtained from the charge density distribution unfolded from the charge distribution of the proton. The same density is assumed for neutrons.

The JLM potential is calculated for the various energies using this 2pF density and the same set of normalization factors $\lambda_v = 1$ and $\lambda_w = 0.8$, which are standard for the light stable nuclei [24]. The resulting calculations for the elastic scattering are presented in Fig. 9 and compared to the data obtained in direct kinematics at 31 MeV [30], 35 MeV [31] and 40 MeV [32]. The JLM calculation is compared to the elastic data we have obtained in inverse kinematics at 36.3 MeV/nucleon in Fig. 8. We obtain a good agreement between the whole set of data and the microscopic calculations done at various energies. This means that our reconstruction method is correct and the efficiency is well estimated.

We measured also the inelastic scattering to the first 2^+ excited state at 4.44 MeV. We calculate the inelastic scattering using the Bohr-Mottelson prescription to build the transition density for ^{12}C. The proton transition density is a derivative of 2pF function (as given by Eq. 4). With the adopted B(E2) value equal to 41 ± 5 e^2.fm^4 [33], the $|M_p|$ moment of the proton density deduced from Eq. 3 is equal to 6.40 ± 0.4 fm^2. From $|M_p| = 6.40$ fm^2 we can fix the normalization of the proton transition density via the integral calculated from Eq. 2. Like the ground state densities, the neutron and proton transition densities are assumed to be identical.

In Fig.8, with the assumption $|M_n| = |M_p| = 6.40 \pm 0.4$ fm^2, the inelastic angular distri-

bution is reproduced with the JLM DWBA calculation, within the error bars. This result shows that the subtraction of the background is well operated, and that the systematical errors on the inelastic cross sections in Sec. II F are correctly estimated.

D. Coupling effects in the case of weakly-bound nuclei

It has been shown [34] that the angular distributions of ^{6}He on proton at energies ranging from 25 to 75 MeV/nucleon, are well reproduced, using the JLM optical potential, provided the real part of the potential be renormalized by a factor 0.8. The origin of this effect was discussed in Ref. [35] : to calculate the interaction potential for elastic scattering, one should include all possible virtual couplings between the ground and excited states. These processes remove flux from the elastic channel. This effect is negligible for stable nuclei, but increases for weakly-bound nuclei. In particular, for exotic isotopes with low particle emission thresholds the coupling between the ground state and the continuum is expected to play an important role. The interaction term arising from couplings to inelastic channels is called the dynamical polarization potential (DPP). It is complex, non-local and energy-dependent [36]. Its exact calculation requires the precise knowledge of the spectroscopy of the nucleus and of the transition strengths to bound and continuum excited states. It is thus difficult to evaluate and is not taken into account in the usual optical model approaches as discussed in Ref. [35]. For that reason, we prefer to approximate its effect in a simpler way with a reduction of the real volume potential V, that is λ_V smaller than 1. Indeed, it was explained in Ref. [37] that a complex surface potential, with a repulsive real part, is expected to simulate the surface effects generated by the DPP. This was found appropriate to understand the elastic scattering data for the ^{6}Li projectile on various targets. The effects induced by the DPP were shown to correspond roughly to the reduction of the real part [37]. Recently, the need for a DPP to analyze the elastic scattering data of the weakly-bound ^{6}He on the ^{12}C target at 38.3 MeV/nucleon was also shown [38].

IV. PROTON ELASTIC AND INELASTIC SCATTERING FOR CARBON ISOTOPES

A. Structure models

We consider two models to generate the densities, AMD [5, 17] and Hartree-Fock formalism with BCS correlations. For this latter model, three types of Skyrme effective interaction were used for the particle-hole (p-h) channel : SIII [39], SGII [40] and Sly4 [41]. A constant gap pairing interaction was used. The transition densities are then calculated with the QRPA which allows to take into account the pairing effects in excited states. The detailed description of these calculations can be found in Ref. [22].

B. Ground state densities

The neutron and proton ground state density distributions calculated within AMD[17] or HF + BCS models are presented in Fig. 10 in linear (left column) and logarithmic (right) scales to view the variations at small and large radii, respectively. The first plots, a. and b. present the comparison between proton and neutron densities for AMD model. The HF + BCS densities with SIII, SGII et SLy4 are presented in Fig. 10 c. d for the proton, and in Fig. 10 e. f for the neutrons. We can compare the neutron and proton ground state densities for the AMD and HF + BCS calculations of ^{10}C. AMD predicts a proton density with a maximum not located at the origin, which is consistent with the clustering of ^{10}C in two α particles and two protons found in this model. In Fig. 11, the same representation is adopted for the ^{11}C ground state densities.
The parameters of the densities (rms for neutron, proton and matter densities) are displayed in Tab. I and II, for ^{10}C and ^{11}C respectively.

C. ^{10}C elastic scattering

In Fig. 12, the elastic scattering data for ^{10}C are compared to the calculations using the JLM potential and densities given within the AMD model and the HF + BCS framework. All the calculations with the standard normalization $\lambda_V = 1.0$, $\lambda_W = 0.8$ (dotted line) overestimate the data at small c.m. angles : this is due to the couplings between the

ground state and the continuum which remove flux from the elastic channel, as seen in Section III D. We simulate that effect by reducing the real part of the potential. The best agreement with experimental data was obtained with a renormalization of the real part of JLM by a factor $\lambda_V = 0.92$, as shown in Fig.12 with the thick solid lines. Taking into account the normalization error on the data, the λ_V range is $\lambda_V = 0.92 \pm 0.03$. We adopt the central value for the analysis. In this case, a good description is obtained with the HF densities, using the SIII and SGII effective interactions.

The angular distribution is correctly reproduced except for the large c.m. angles which are underestimated in the AMD model and HF + BCS with the SLy4 effective interaction. Since these two calculations are associated with the largest rms matter radius, it means that a slightly smaller rms radius is needed. The HF + BCS densities (SIII and SGII) allowing the best reproduction of the elastic angular distributions gave a neutron rms radius of 2.3 ± 0.01 fm and a larger proton rms radius of 2.5 ± 0.03 fm. In the following subsection we will discuss the sensitivity of the elastic scattering to the matter rms radius.

D. Sensitivity of the method and extraction of the rms radius for ^{10}C

Since the angular range in our measurement does not exceed $50^\circ_{c.m.}$, the elastic cross sections are mainly sensitive to the matter rms radius. This is illustrated in Fig. 13a. by a calculation done using, for simplicity, gaussian-function densities for ^{10}C with two different values r_m= 2.3 or 2.45 fm. Fig. 13b presents calculations using two densities of the same $r_m = 2.45$ fm, having the same (thick line) or different (dashed line) values for the neutron and proton radii. Obviously, elastic scattering data are not sensitive to these small differences in the neutron-proton densities. For ^{10}C the HF+BCS(SGII) densities give a satisfactory agreement. They can easily be fitted by a 2pF function. Consequently, to deduce the rms of the ^{10}C from the data, we use the 2pF parameterization from Eq.5 for the proton and neutron density distributions, and the parameters of the radius R_o, diffuseness a and ρ_o are obtained applying the following prescriptions : ρ_o is calculated in order to normalize the proton and neutron densities to the values of the neutron N and proton Z numbers of ^{10}C, R_o and a are fixed initially to the value of the experimental ^{12}C proton density (Sec. III C), then they are varied so as to provide a profile for the proton and neutron distributions close to the HF+BCS (SGII) densities, and same proton and neutron rms radii as the ones of

SGII densities (given in Tab.I).

The final parameters of the fitted 2pF densities are given in Tab.III. The rms radii of these functions are close to those of the initial densities, those are 2.31 fm for neutrons and 2.50 fm for protons. The rms radius of the resulting matter density is $r_m = 2.42$ fm. From calculations with 2pF functions which correctly reproduce the angular distribution, we deduce the central value and error bar on the rms value : $r_m = \sqrt{< r^2 >_m} = 2.42 \pm 0.10$ fm.

The error bar takes into account the statistical error on data, the uncertainty on λ_V and the different values obtained in calculations which reproduce equally well the data. This extracted value is within the same range as the ^{12}C one, showing that the ^{10}C nucleus has a similar matter extension, even with less neutrons than ^{12}C.

The AMD ground state densities do not give a good description of the elastic scattering at the large angles, but this can be due to the underestimation of the correlations between alpha-clusters, resulting in an overestimation of the neutron extension, and then of the matter rms radius. The HF+BCS calculation, validated by the elastic data, predicts for r_p significantly larger values than for r_n in Table I.

E. ^{11}C elastic scattering

In the same way as for ^{10}C, we need a reduction of the real potential, here with $\lambda_V = 0.90 \pm 0.03$, to reproduce the ^{11}C + p elastic scattering distribution at small c.m. angles, whatever the adopted densities, either from AMD or HF + BCS models. The comparison between the data and these calculations is shown in Fig. 14.

However the data at larger angles are not reproduced in any calculation, suggesting a rms matter radius smaller than expected. Since the elastic scattering in the angular range we measured is not sensitive to the difference of shape between neutron and proton as shown in Sec.IV D, the ground state density is parametrized with a 2pF function with the same geometry for the neutron and proton densities. We adopt the same procedure as used for ^{10}C density, and deduce the 2pF parameters for proton and neutron densities providing the best agreement with the elastic data. These parameters are displayed in Tab.III.

This allows also to obtain the matter rms radius for ^{11}C : $r_m = 2.33 \pm 0.1$ fm, very close to the value for the neighbour ^{12}C, slightly larger than the values deduced from interaction

cross sections [8].

For ^{10}C, as well as for ^{11}C, the best agreement with the data is obtained using densities having a smaller rms radius than the one predicted by the AMD calculations. A 2pF profile with parameters adjusted to reproduce the data was found to provide a satisfactory agreement.

F. ^{10}C inelastic scattering to the first 2^+ states

The elastic cross sections provide the entrance channel potential used throughout the analysis of the inelastic cross sections. For the whole inelastic scattering analysis, and to calculate the elastic and transition form factors, the λ_V factor deduced from the elastic data will be fixed to 0.92 for ^{10}C and to 0.90 for ^{11}C.

Different densities are considered here to calculate the JLM potentials : the AMD predictions and the QRPA densities plotted in Fig. 15. The corresponding $|M_n|$, $|M_p|$, B(E2) and M_n/M_p values are given in Tab.IV. The transition density from the first 0^+ state to the first 2^+ state in ^{10}Be has already been calculated in the AMD framework [42]. In these calculations, $B(E2; 0_1^+ \rightarrow 2_1^+) = 55$ e^{2}fm^4 in ^{10}Be, close to the experimental value : $B(E2; 0_1^+ \rightarrow 2_1^+) = 52.5 \pm 5$ e^{2}fm^4 [9]. The authors assume mirror symmetry between ^{10}C and ^{10}Be to calculate the $B(E2; 0_1^+ \rightarrow 2_1^+)$ of ^{10}C, found in their model to be equal to 45 e^{2}fm^4. By analysing the intrinsic state of the wave function of the main component, they found that the deformations of proton and neutron are different, larger for the proton density than for the neutron one, deformed as triaxial. This AMD B(E2) is at 1.6σ from the experimental value, higher than the predicted QRPA B(E2) values. All these calculations underestimate the known B(E2) value, even though the error bar on B(E2) are large. In Fig.16, using AMD and QRPA, the JLM calculations for the inelastic scattering to the first 2^+ excited state at 3.35 MeV are compared to our data. Neither the AMD transition densities [5] nor the QRPA incorporated in our JLM calculations allow to reproduce the inelastic (p,p') data.

The experimental adopted B(E2) value is known, B(E2) $= 61.5 \pm 10$ e^2.fm^4 [9], and the proton integral can be deduced from Eq.3 : $M_p = 7.84 \pm 0.64$ fm^2. A possible approach could be to use the AMD or the QRPA densities and to renormalize the calculated proton transition density to the experimental value of M_p (Eq. 2). The normalization of the neutron transition density could then be adjusted in order to fit the (p,p') data.

The proton and neutron excitations in AMD are rather close to the experimental values (see Tab. IV), but since the elastic data analyzed using the AMD ground state densities were not reproduced at larger angles (Sec. IV C) we choose to deduce the M_n value using a parameterization for the neutron and proton transition densities.

We proceed to determine the M_n value using the Bohr-Mottelson prescription, formulated in Ref. [12] : the ground state densities are derived according to the Tassie formula (Eq.4), in order to obtain the transition densities. These ground state densities are chosen according to the results explained in Sec. IV D. Since the HF+BCS densities with SGII interaction were validated by the elastic scattering data (with $\lambda_V = 0.92$), and the 2pF functions adjusted on these densities were found to be consistent with the data, for simplicity, we can use this parameterization of the proton and neutron ground state densities to generate the transition densities. The normalization of the proton transition density is fixed on the M_p central value $M_p = 7.84$ fm^2, and the neutron normalization can be adjusted on the (p,p') data or fixed on a given value, to test different assumptions.

In Fig. 17, we show calculations, with the same renormalized proton transition density ($M_p = 7.84$ fm^2), and two different $|M_n|$ values : a reasonable agreement is obtained with the ratio $|M_n|/|M_p| = \mathrm{N/Z}$ (short dashed line) while the best agreement corresponds to $|M_n|/|M_p| = 0.70 \pm 0.08$ (solid line). Taking into account the error bar on the $|M_p|$ value and on the extraction of the M_n/M_p value from the data, we deduce $|M_n| = 5.51 \pm 1.09$ fm^2. This is in contrast with the AMD and QRPA models which both predict a ratio M_n/M_p greater than 1. The experimental result indicates that the contribution to the excitation from the protons is larger than from neutrons, as can be expected from the Z/N ratio.

The AMD calculation directly assumes mirror symmetry in the T=1 A=10 isospin doublet to deduce the neutron densities of ^{10}C from the proton density of ^{10}Be. The prediction of the B(E2) is closer to the experimental value than the ones from the QRPA model, but the neutron excitation is clearly overestimated : $M_n(\mathrm{AMD}) = 7.42$ fm^2. The $M_n/M_p(^{10}\mathrm{C})$ ratio can be merely calculated by assuming the mirror symmetry : we consider $M_n(^{10}\mathrm{C}) = M_p(^{10}\mathrm{Be})$, with $M_p(^{10}\mathrm{Be}) = 7.245 \pm 0.345$ fm^2, deduced from the experimental B(E2) value ($52.5 \pm 5.$ e^{2}fm^4), and we obtain $M_n/M_p(^{10}\mathrm{C}) = M_p(^{10}\mathrm{Be})/M_p(^{10}\mathrm{C}) = 0.92$ with an error bar of ± 0.13. Comparing this ratio to the one deduced from (p,p'), and the M_n value from mirror symmetry, equal to 7.245 ± 0.345 fm^2, to the measured $|M_n| = 5.51 \pm 1.09$ fm^2,

the mirror symmetry is not fulfilled in the $T = 1, A = 10$ nuclei ^{10}Be and ^{10}C.

The full discussion of the symmetry breaking effects between ^{10}Be and ^{10}C will be the subject of a forthcoming article devoted to the quantitative tests on proton and neutron transition matrix elements of ^{10}C and ^{10}Be.

G. ^{11}C inelastic scattering to the $5/2^-$ and to the $7/2^-$ states

If we consider the spectroscopy of ^{11}C in Fig. 1, we can see that, around 4.5 MeV, two excited states can be found, a $5/2^-$ at 4.3 and a $3/2^-$ at 4.8 MeV. In the energy range from 6 to 7 MeV we have also several states as shown in Fig. 1 : $1/2^+$, $7/2^-$, $5/2^+$. In Fig. 7, the comparison of the peaks observed for ^{11}C(p,p') with the 2^+ peak obtained for ^{10}C shows similar widths. Moreover, considering the experimental resolution measured on the elastic peak (700 keV), we can assume that one state of the doublet is mainly contributing to the (p,p') excitation between 4 and 5 MeV, that is, the $5/2^-$; between 6 and 7 MeV, we attribute the peak to the $7/2^-$ state. In the following, to discuss the ^{11}C cross sections, we assume that the (p,p') reaction at 40 MeV/nucleon mainly selects the transitions from ground to $5/2^-$ (4.3 MeV) and to $7/2^-$ (6.48 MeV) states.

These transitions are expected to be electric quadrupolar $E2$ transitions in the AMD model. The values of the moments $|M_n|$, $|M_p|$ and B(E2) obtained with these densities can be found in Tab. V. The proton and neutron transition densities from AMD are presented in Fig. 18. It should be noted that, clearly, it cannot be expected that the simple QRPA model could provide a good treatment of the excited states of such a light odd-even nucleus as ^{11}C. The time-reversal symmetry is broken and the blocking approximation should be careful treated. The theoretical cross sections have been calculated with the JLM potential including AMD densities. Using these predicted $E2$ transitions, the calculated (p,p') angular distributions are found to be consistent with the shape of the experimental angular distribution presented in Fig. 19. The AMD densities allow to give the correct order of magnitude for the cross sections. The reproduction of the experimental cross sections is satisfactory.

However, in contrast with the analysis done for ^{10}C, since the experimental B(E2) values are not known, the inelastic scattering data cannot give access to the $|M_n|$ factor, it only allows to check the theoretical transition densities. It should be noted that within usual

mean-field models (for instance the present QRPA), with no specific treatment of the light odd-even nuclei, the predicted $|M_n|$, $|M_p|$ and B(E2) values are very small. Then, the resulting JLM calculations using these mean-field transition densities underestimate strongly the inelastic cross sections. For both transitions, the AMD model was found to give a rather good agreement with the data, which would validate the AMD model, in spite of some disagreement with the elastic scattering data due to a too large rms matter radius. The Coulomb excitation represents a complementary measurement, which would allow to fix the contribution of the proton to the ^{11}C excitation and the proton integral $|M_p|$ for the ground to $5/2^-$ (4.32 MeV) and $7/2^-$ (6.48 MeV) states and to progress in the extraction of the neutron excitation from the (p,p') analysis. Nevertheless, the experimental value for the global isoscalar $M_n + M_p$ value can be obtained from this (p,p') analysis. It is indicated in Tab. V.

In the mass region of the p-shell nuclei, the microscopic models usually underestimate the nucleon excitations. The resulting predicted values of the E2 transition or quadrupole moments are usually too small, compared to the experimental ones. For instance, the authors of Ref. [43] underlined that the values predicted by their shell model calculations were underestimated, and they had to change the effective charges to improve the agreement. The fact that the AMD calculations give the order of magnitude for the (p,p') scattering for the odd-even ^{11}C, and predict a rather high value for the B(E2) of ^{10}C, favours this model for further microscopic studies of these nuclei.

V. CONCLUSIONS

We have presented the analysis of the ^{10,11}C(p,p') scattering data, measured in inverse kinematics with radioactive beams. From the energy, time of flight and position of the light charged particle, allowing for an identification of the light particles, in coincidence with the ejectile in the plastic wall, a full reconstruction of the (p,p') kinematics was possible in the angular range from 10 to $50^\circ_{c.m.}$. Using beam detectors, an energy resolution of 700 keV was achieved, enough to separate elastic from inelastic contributions.

The ^{12}C(p,p') cross sections were measured at an energy of 36.3 MeV/nucleon, in the same conditions as the ^{10,11}C ones. This allowed to cross-check the reconstruction, the background suppression and the normalization. We have extracted the experimental distributions for

the proton elastic scattering of ^{11}C at 40.6 MeV/nucleon and for inelastic scattering to the $5/2^-$ (4.32 MeV) and $7/2^-$ (6.48 MeV) ^{11}C states, for elastic scattering data of ^{10}C+p at 45.3 MeV/nucleon and inelastic scattering to the 2^+ state of ^{10}C.

The (p,p') analysis was performed within the microscopic nucleus-nucleon potential approach, using the JLM microscopic potential. The coupling effects induced by the weak binding of the unstable nuclei on the interaction potential were taken into account by reducing the real part of the potential. The potential in the entrance channel of (p,p') reactions was tuned on the elastic scattering. Direct structure information (matter rms radii, neutron moment for ^{10}C) was extracted. The elastic data were found consistent with an extended matter rms radius of 2.42 $\pm$ 0.1 fm for ^{10}C, comparable with the rms of the heavier ^{12}C (2.3 $\pm$ 0.1 fm). It is found to be 2.33 ± 0.1 fm for ^{11}C. We have proposed 2pF profiles for the densities of ^{10}C and ^{11}C, consistent with the elastic data, the parameters are given in Tab. III.

The validity of the models was discussed : we have tested the ground and transition densities predicted by HF+BCS and QRPA and by cluster-model calculations. The matter rms radius for ^{10}C was overestimated by AMD, and both models overestimated the rms matter radius for ^{11}C. HF+BCS (for the SIII and SGII interactions) provided a good agreement with the ^{10}C elastic data. Both AMD and QRPA fail in reproducing correctly the ^{10,11}C(p,p') data. This means that an appropriate framework beyond QRPA mean-field should be developed to describe the excitations of light odd-even nuclei like ^{11}C. In the AMD model, an improvement of the theoretical description of the proton-neutron correlations could be required.

In the case of the ^{11}C(p,p'), prior to our measurement, the transition multipolarities for ^{11}C from ground state to $5/2^-$ at 4.32 MeV and $7/2^-$ at 6.48 MeV were unknown. The shape of the experimental angular distributions are very similar to those calculated by considering electric quadrupolar $E2$ transition.

The proton inelastic scattering probe is a powerful tool to investigate the profile of the density and to extract the moment of the neutron transition density : within the covered angular range, the proposed 2pF density, and the derived transition density were validated on the analysis of the elastic and inelastic scattering, and the M_n factor for ^{10}C was deduced. The M_n/M_p ratio is 0.70 ± 0.08, indicating a stronger contribution from the protons in the E2 excitation, this effect is not predicted by the models considered in this article. This value

is not in agreement with the value expected when assuming the mirror symmetry. But, for such a light neutron-deficient system as ^{10}C, the Coulomb effect is expected to be important and could be mainly responsible of the isospin symmetry breaking. Detailed tests of mirror symmetry for the 2^+_1 excitations of the T=1 ^{10}C-^{10}Be isospin doublet will be done on the ^{10}C(p,p') data and reported in a later publication.

Acknowledgments

We thank Dr Y. Kanada En'yo for providing us with her ^{10,11}C density distributions. The help of P. Gangnant, J.F. Libin (GANIL) during the preparation of the experiment, of C. Mazur and M. Riallot (Dapnia/SEDI) for the CATS detectors, of L. Petizon (IPN-Orsay) for the mounting of the MUST detectors is gratefully acknowledged.

---

[1] R. C. Barrett and D. F. Jackson, Nuclear Sizes and Structure (Clarendon, Oxford, 1977).

[2] K. Ikeda, N. Tagikawa and H. Horiuchi, Prog. Theor. Phys. (Jap), Suppl. (1968) 464.

[3] W. von Oertzen, Z. Phys. A **357** (1997) 355, Physica Scripta **T88** (2000) 83.

[4] M. Freer *et al.*, Phys. Rev. C **49**, 1751 (1994).

[5] Y. Kanada-En'yo and H. Horiuchi, Phys. Rev. C **55**, 2860 (1997) and ref. therein.

[6] F. Ajzenberg-Selove, Nucl. Phys. **A 490** (1988) 1., *ibid.* **A 506** (1990) 1.

[7] A. Ozawa, I. Tanihata, T. Kobayashi, Y. Sugahara, O. Yamakawa, K. Omata, K. Sugimoto, D. Olson, W. Christie, and H. Wieman, Nucl. Phys. A**608** (1996) 63.

[8] A. Ozawa *et al.*, Nucl. Phys. A**583** (1995) 807.

[9] P. Raghavan, At. Data Nucl. Data Tables 42, 189 (1989).

[10] A. Lagoyannis *et al.*, Phys. Lett. B **518**, 27 (2001).

[11] A.M. Bernstein, V.R. Brown and V.A. Madsen, Phys. Rev. Lett. **42**, 425 (1979).

[12] G. R. Satchler, *Direct Nuclear Reactions* (Clarendon Press, Oxford 1983).

[13] P. D. Cottle *et al.*, Phys. Rev. Lett. **88**, 172502 (2002).

[14] P. D. Cottle *et al.*, Phys. Rev. C **60**, 031301 (1999).

[15] E. Khan, V. Lapoux, N. Alamanos and Y. Blumenfeld, Phys. Rev. C **69**, 031303 (1999).

[16] J.P. Jeukenne, A. Lejeune and C. Mahaux, Phys. Rev. C **16**, 80 (1977).

[17] Y. Kanada-En'yo, private communication.

[18] Y. Blumenfeld *et al.*, NIM **A 421** (1999) 471-491.

[19] A. Joubert *et al.*, Particle Accelerator Conference IEEE Vol 1 (1991) 594.

[20] J. L. Baelde *et al.*, Nouvelles du GANIL, n^0 44, fév. 1993.

[21] S. Ottini *et al.*, NIM A **431**, 476 (1999).

[22] E. Khan *et al.*, Phys. Lett. B. **490**, 45 (2000).

[23] S. Mellema, R. Finlay, F. Dietrich and F. Petrovich, Phys. Rev. C **28**, 2267 (1983).

[24] J. S. Petler *et al.*, Phys. Rev. C **32**, 673 (1985).

[25] N. Alamanos, F. Auger, B. A. Brown and A. Pakou, J. Phys. G 24 (1998) 1541.

[26] N. Alamanos and A. Gillibert, *Selected topics in Reaction Studies with Exotic Nuclei*, Lect. Notes Phys. **651**, 295-337 (2004).

[27] T. Tamura, W.R. Coker and F. Rybicki, Comp. Phys. Commun. **2**, 94 (1971).

[28] M. El-Azab Farid and G. R. Satchler, Nucl. Phys. **A438**, 525 (1985).

[29] H. De Vries, C. W. De Jager, and C. De Vries, At. Data Nucl. Data Tables 36, 495 (1987).

[30] J. Kirk Dickens *et al.*, Phys. Rev. **129**, 743 (1963).

[31] R. De Leo *et al.*, Phys. Rev. C **28**, 1443 (1983).

[32] L. N. Blumberg *et al.*, Phys. Rev. **147**, 812 (1966).

[33] S. Raman *et al.*, At. Data and Nucl. Data Tables 36 (1987) 1.

[34] V. Lapoux *et al.*, Phys. Lett. B **517**, 18 (2001).

[35] M.E. Brandan and G. R. Satchler, Phys. Rep. **285**, 143 (1997).

[36] H. Feshbach, Ann. Phys. **5**, 357 (1958).

[37] Y. Sakuragi, Phys. Rev C **35**, 2161 (1987).

[38] V. Lapoux *et al.*, Phys. Rev. C **66**, 034608 (2002).

[39] M. Beiner, H. Flocard, Nguyen Van Giai and P. Quentin, Nucl. Phys. **A238**, 29 (1975).

[40] Nguyen Van Giai and H. Sagawa, Nucl. Phys. **A371**, 1 (1981).

[41] E. Chabanat, P. Bonche, P. Haensel, J. Meyer, and F. Schaeffer, Physica Scripta **T 56**, 231 (1995) ; Nucl. Phys. A635, 231 (1998).

[42] Y. Kanada En'yo *et al.*, Phys. Rev. C **60**, 064304 (1999).

[43] P. Navràtil, W. E. Ormand, Phys. Rev. C **57**, 3119 (1998).

	AMD	HF+BCS			Exp [7]
		SIII	SGII	SLy4	
$r_n\,(fm)$	2.50	2.29	2.31	2.37	2.22 ± 0.03
$r_p\,(fm)$	2.57	2.53	2.52	2.61	2.31 ± 0.03
$r_m\,(fm)$	2.55	2.44	2.44	2.51	2.27 ± 0.03

TABLE I: Rms neutron r_n, proton r_p and matter r_m radii obtained for the ^{10}C densities presented in Fig. 10. They are compared to the values deduced from experiments in Ref. [7].

	AMD	HF+BCS			Exp [8]
		SIII	SGII	SLy4	
$r_n\,(fm)$	2.43	2.39	2.39	2.45	2.10 ± 0.06
$r_p\,(fm)$	2.48	2.48	2.48	2.54	2.13 ± 0.06
$r_m\,(fm)$	2.46	2.44	2.44	2.50	2.12 ± 0.06

TABLE II: Rms for neutron (r_n), protons r_p and matter r_m densities calculated with the ^{11}C densities presented in Fig. 11. They are compared to the previous experimental values from [8].

	^{10}C				^{11}C			
	ρ_o	R_o	a	rms	ρ_o	R_o	a	rms
	fm^{-3}	(fm)			fm^{-3}	(fm)		
proton	0.0929	2.16	0.499	2.50	1.104	2.06	0.455	2.33
neutron	0.0808	1.96	0.469	2.31	0.092	2.06	0.455	2.33
r_m (fm)	2.42 ± 0.1				2.33 ± 0.1			

TABLE III: Parameters of the 2pF ground state proton and neutron densities for ^{10}C and ^{11}C, allowing to reproduce the elastic scattering data.

	Exp [9]	AMD	QRPA			This work
			SIII	SGII	SLy4	
$M_n\,(fm^2)$		7.42	5.15	6.01	5.96	5.51 ± 1.09
$M_p\,(fm^2)$	7.84 ± 0.64	6.71	4.65	5.50	4.70	
$B(E2)\,(e^2fm^4)$	61.5±10	45	21.62	30.27	22.07	
M_n/M_p		1.11	1.11	1.09	1.27	0.70±0.08

TABLE IV: Transition matrix elements M_n, M_p and reduced transition strength for the E2 transition from 0^+ ground to first 2^+ excited state of ^{10}C. The transition densities are presented in Fig. 15.

	AMD			Exp., this work
	$M_n\,(fm^2)$	$M_p\,(fm^2)$	$B(E2)\,(e^2fm^4)$	$\lvert M_n + M_p\rvert\,(fm^2)$
gs to $5/2^-$	7.84	6.60	10.88	16.2 ± 1.7
gs to $7/2^-$	2.99	7.87	15.48	13.3 ± 2.5

TABLE V: Transition matrix elements M_n, M_p and reduced transition strength for the E2 transitions from the $3/2^-$ ground to $5/2^-$ (E^*=4.32 MeV) excited state and for the ground state to $7/2^-$ (E^*=6.48 MeV) of ^{11}C. The experimental values $M_n + M_p$ extracted from the present (p,p') data are given in the last column.

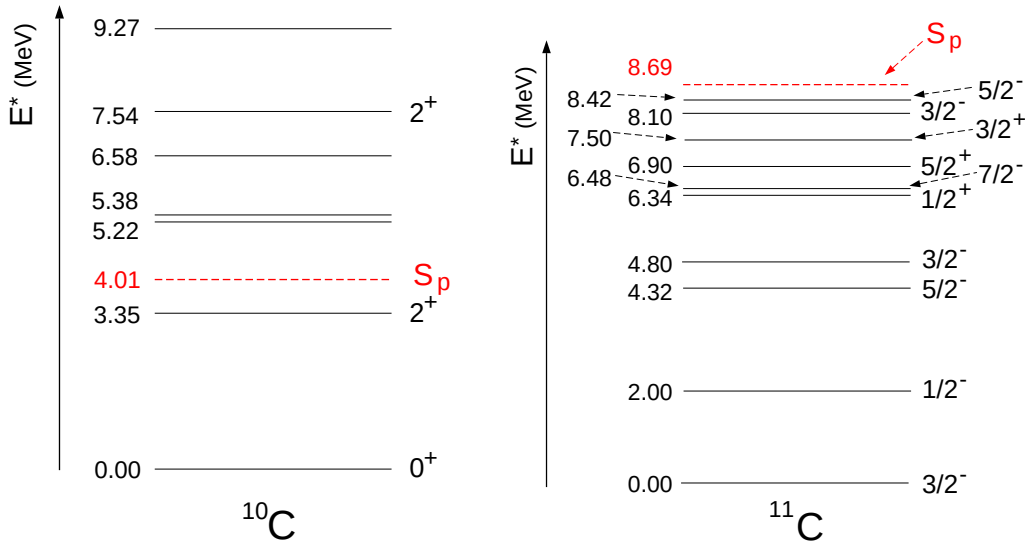

FIG. 1: (Color online) Spectroscopy of ^{10,11}C obtained from tables given in Ref. [6].

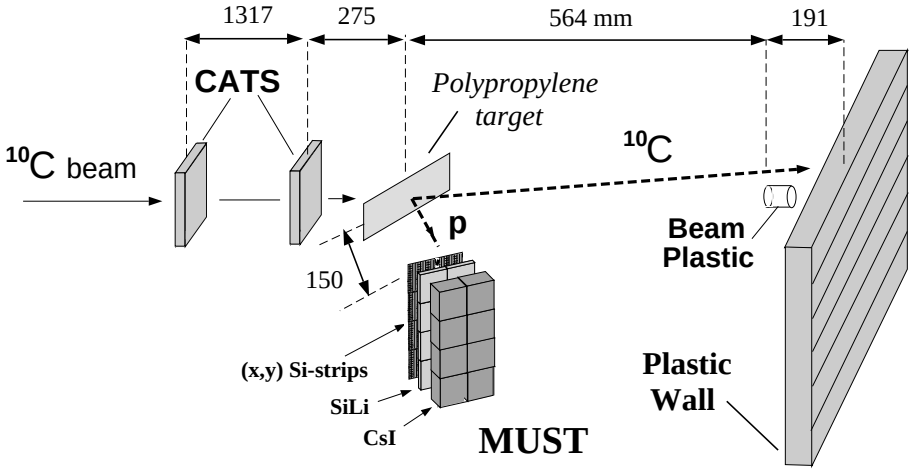

FIG. 2: Experimental setup in the reaction chamber.

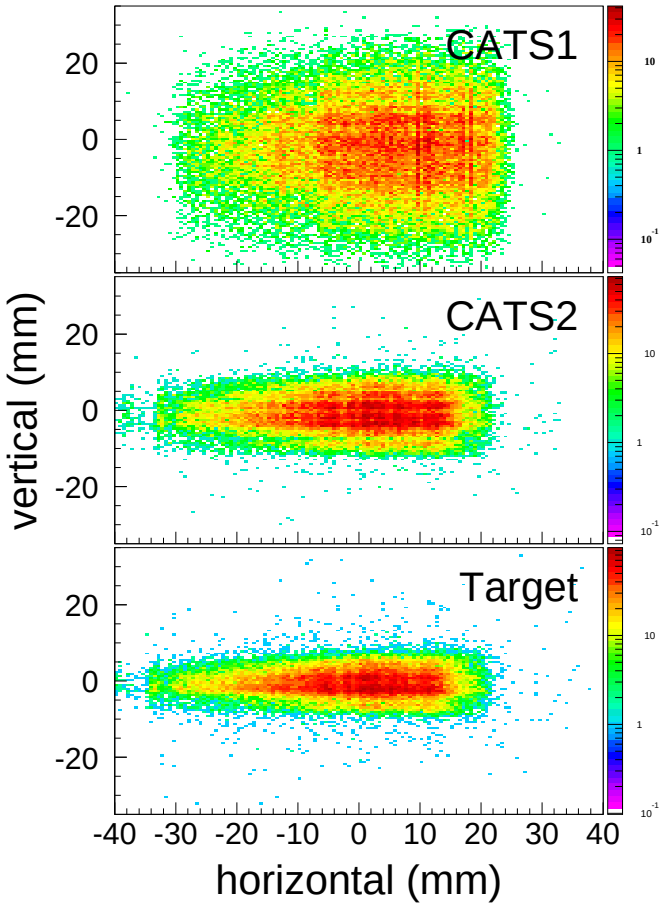

FIG. 3: (Color online) From top to bottom : beam profiles on detectors CATS1 and CATS2, reconstructed beam profile on the target.

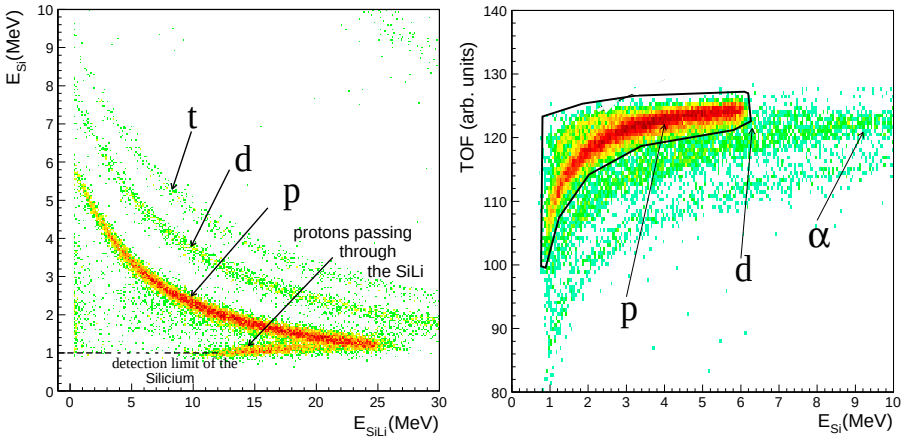

FIG. 4: (Color online) Identification spectrum of the light charged particles in the MUST array, by E-ΔE (left) and by E-TOF techniques (right panel).

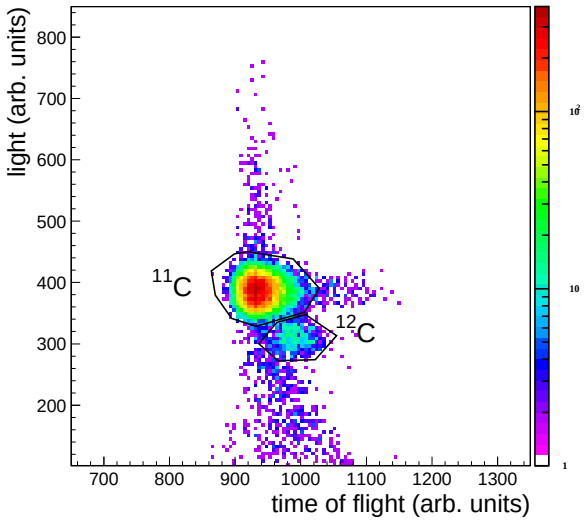

FIG. 5: (Color online) Identification spectrum of ^{11}C particles from the correlation matrix between the light deposited in the Faraday plastic versus the TOF measured between the plastic and the CATS2 beam detector.

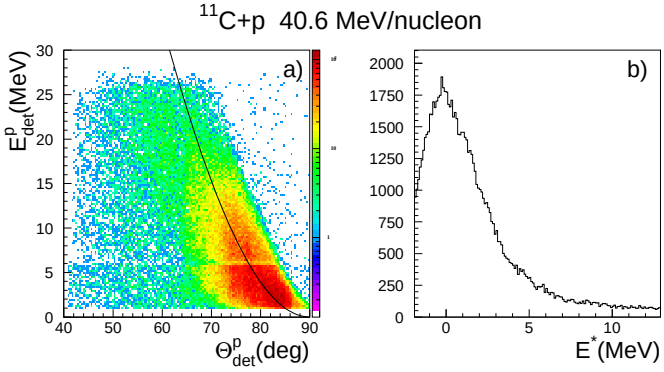

FIG. 6: (Color online) Uncorrected scattering matrix $(\theta^p_{lab}; E^p_{lab})$ for the reaction ^{11}C +p at 40.6 MeV/n and ^{11}C excitation energy spectrum. The incident angle and beam impact on the target given by the CATS are not taken into account.

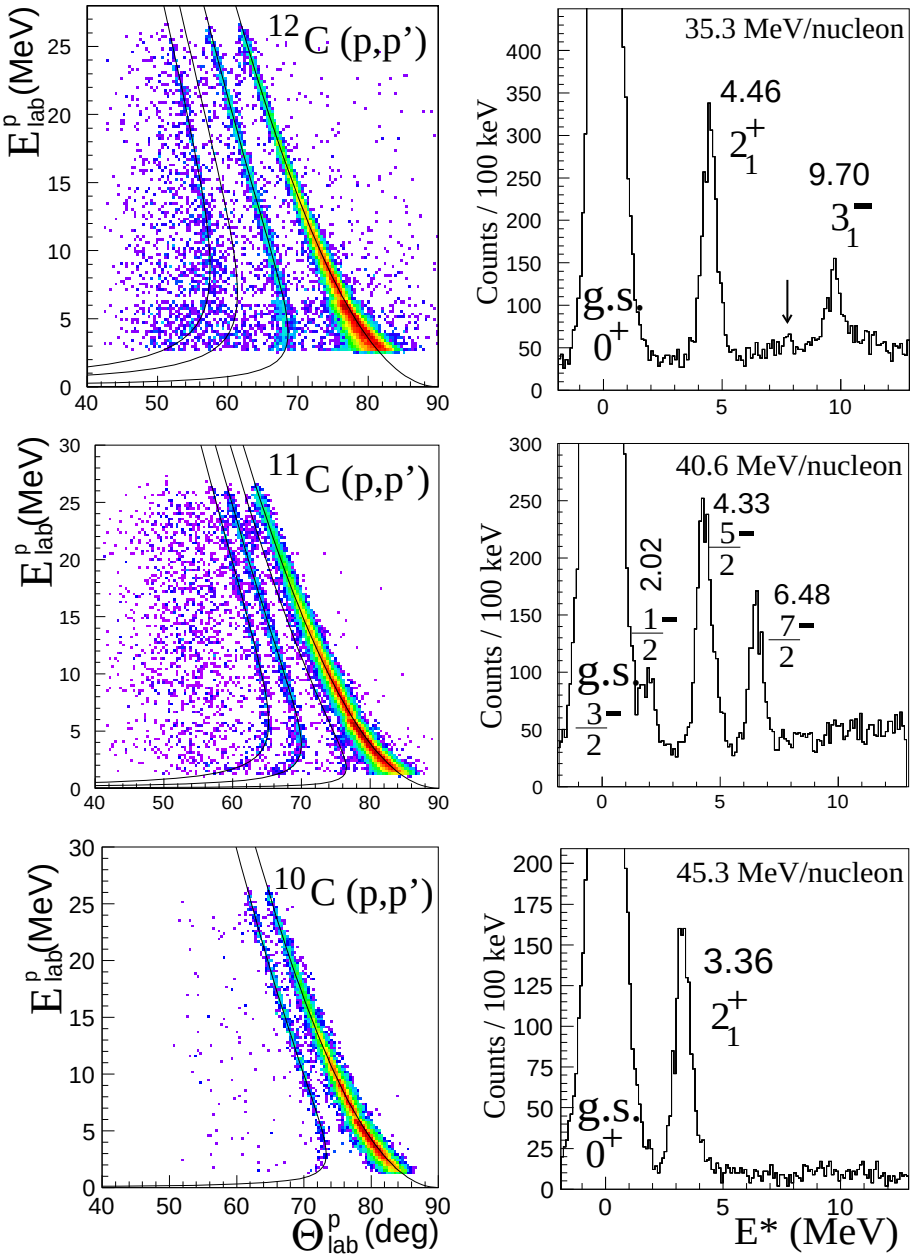

FIG. 7: (Color online) From top to bottom, elastic and inelastic scattering data for ^{12,11,10}C on proton at 35.3, 40.6 and 45.3 MeV/nucleon, respectively. The 8.25 mg/cm^2-thick target was used for these ^{12}C(p,p') events, the 1.48 mg/cm^2-thick one for ^{10,11}C(p,p') shown here. Left column is for the correlation matrices of the proton energy deposited in the Si-strip and SiLi stages versus the angle measured in the lab. frame, θ_{lab}. The thick lines superimposed are the kinematical loci of the (p,p') reaction to the ^{11}C states. Right side column gives the corresponding excitation energy spectrum in the energy range up to 13 MeV. For ^{12}C (first line) the position of the 0^+_2 state, weakly excited by the (p,p') is only indicated by a vertical arrow. For ^{11}C (^{10}C), no structure over the one-proton separation energy can be seen due to the imposed with ^{11}C (^{10}C) in the plastics.

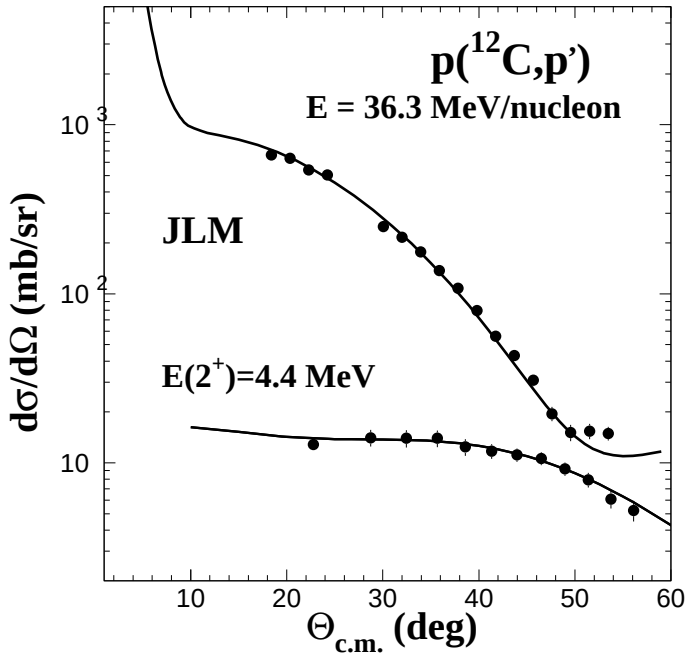

FIG. 8: Elastic and inelastic scattering data for ^{12}C on proton target at 36.3 MeV/nucleon in comparison with the results given by the JLM microscopic potential calculated using densities described in the text.

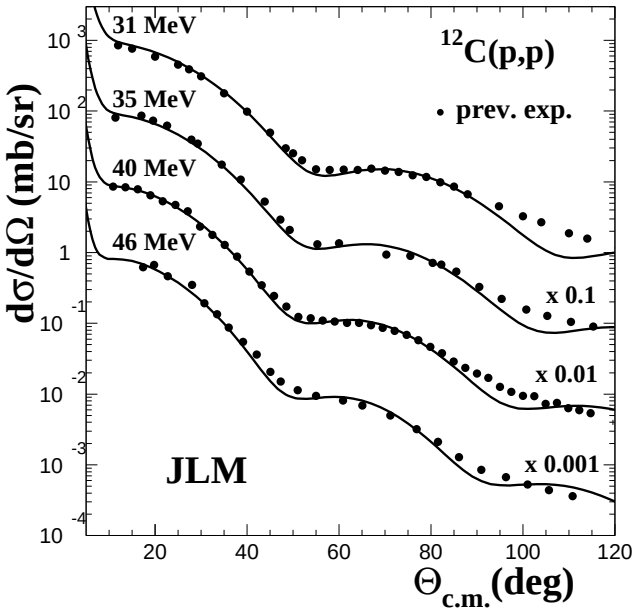

FIG. 9: Comparison of the elastic scattering data for ^{12}C on proton target at various energies (references can be found in the text) in comparison with the results given by the JLM microscopic potential calculated using the ^{12}C 2pF density. The standard normalization of the JLM imaginary potential ($\lambda_w = 0.8$) for light nuclei is applied.

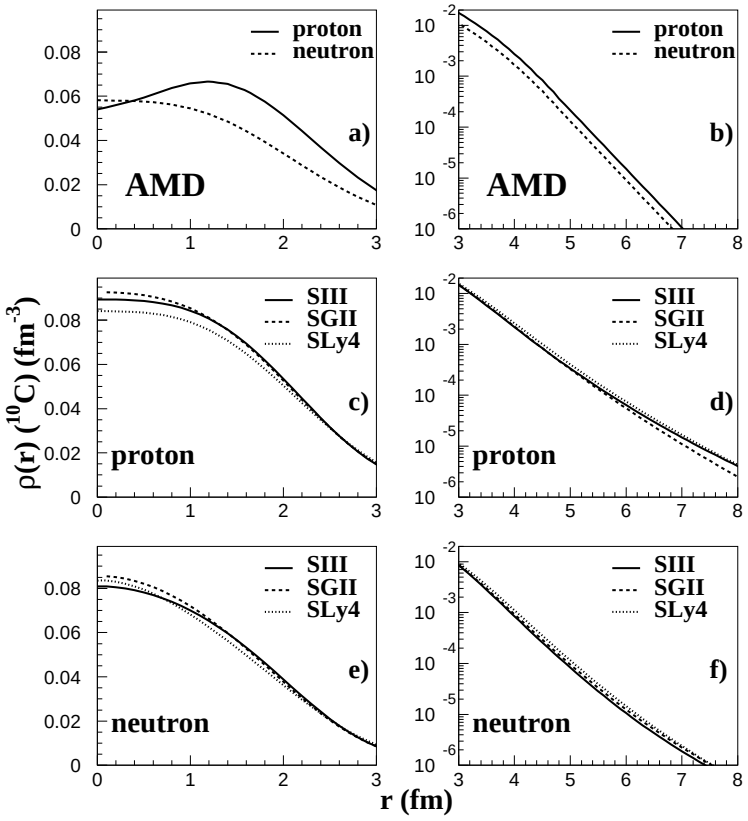

FIG. 10: Neutron and proton ground state densities for ^{10}C obtained with the AMD model (a and b) and the HF+BCS calculations done with three Skyrme interactions (c to f). The densities in the left (right) column are displayed in linear (logarithmic) scale.

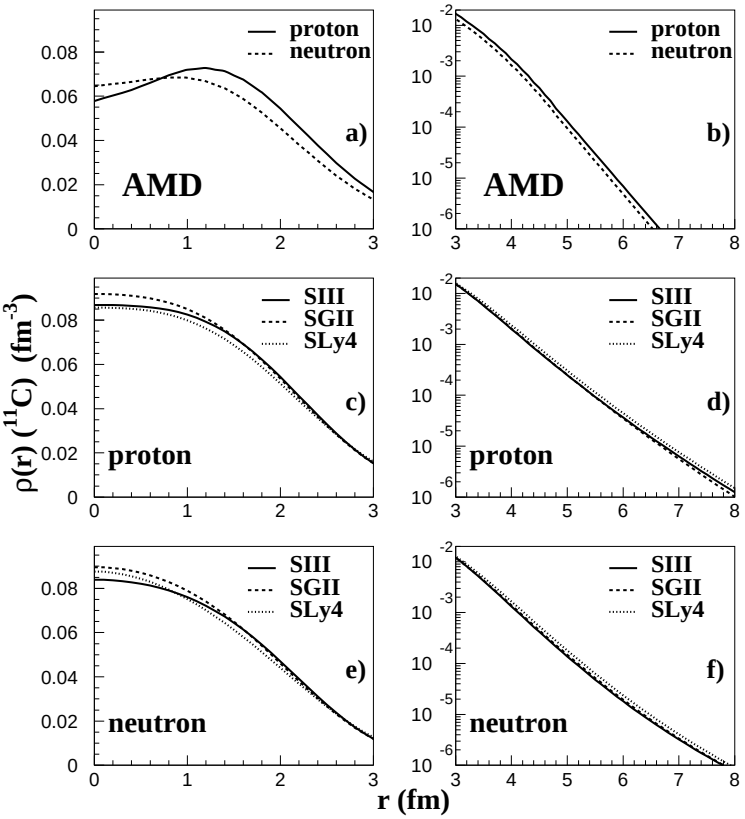

FIG. 11: Same as in Fig.10 for ^{11}C ground state densities.

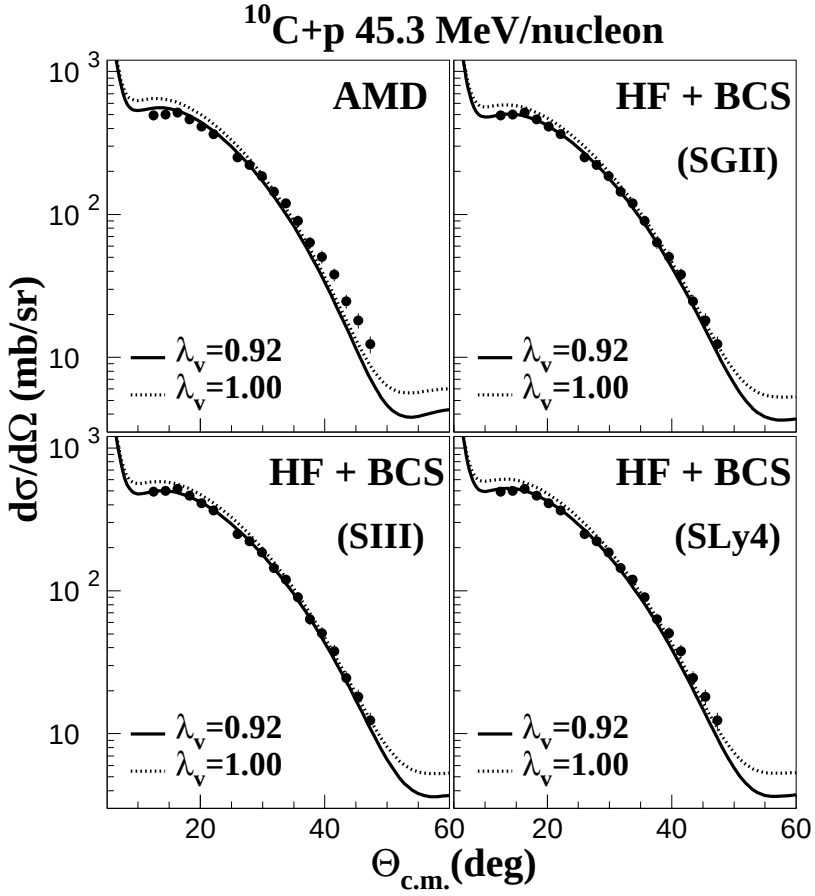

FIG. 12: Elastic scattering data for ^{10}C on proton target at 45.3 MeV/nucleon in comparison with the results given by the JLM microscopic potential calculated with the AMD and HF densities. Three Skyrme forces (SGII, SIII, SLy4) were considered for the HF calculations. The solid and dotted lines are obtained with a normalization factor for the real part equal to 0.92 and 1, respectively.

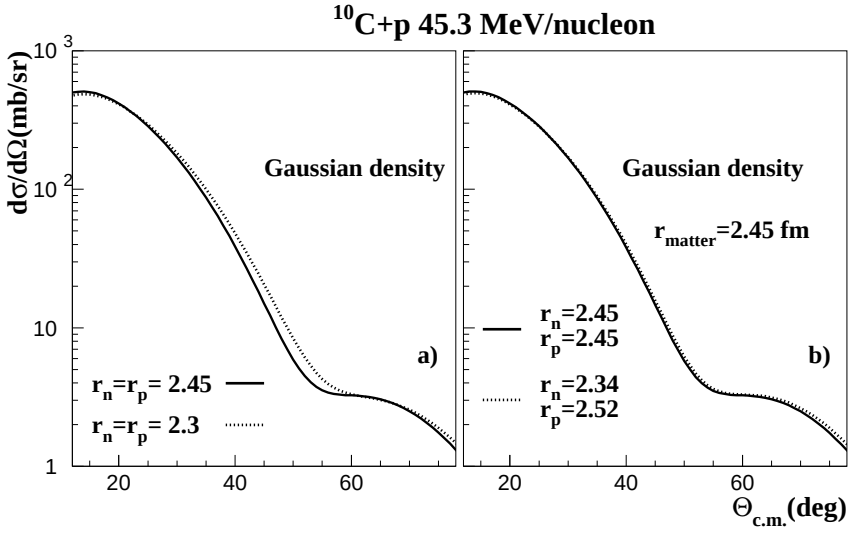

FIG. 13: JLM calculation for ^{10}C+p elastic scattering at 45.3 MeV/nucleon using gaussian-function densities : a) with equal proton and neutron densities, one having a rms radius equal to 2.45 fm (solid line), other with 2.3 fm (dotted line) and b) two matter densities with same rms radius (2.45 fm) but different r_n and r_p.The normalization factor for the real part is fixed to 0.92.

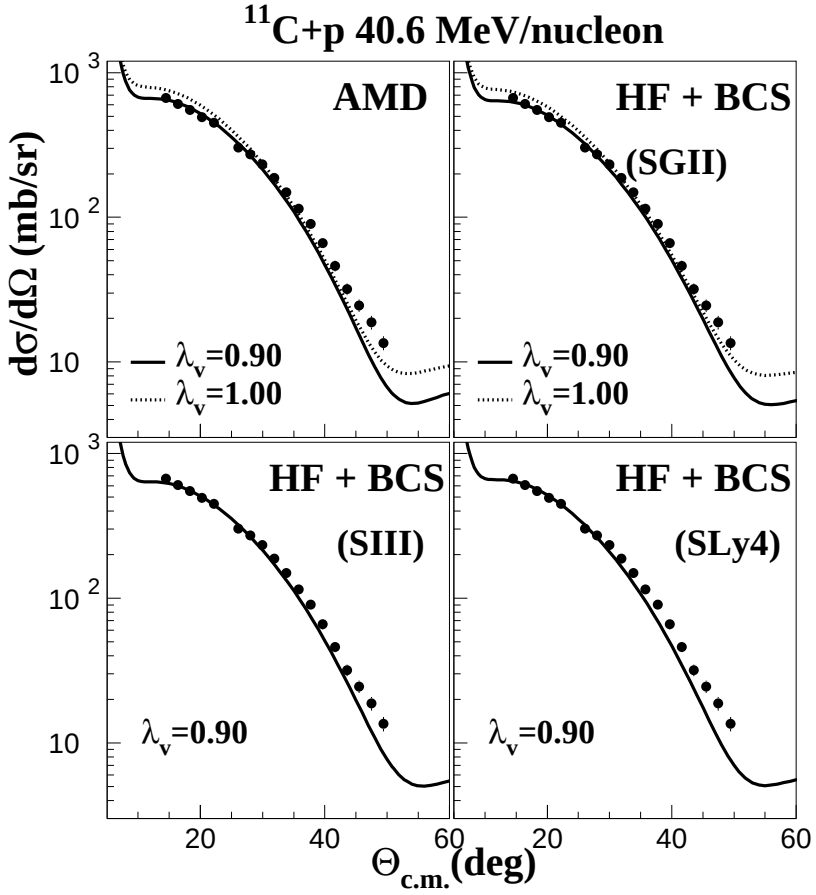

FIG. 14: Same as in Fig.12 for ^{11}C. The solid and dotted lines are obtained with a normalization factor for the real part equal to 0.9 and 1, respectively.

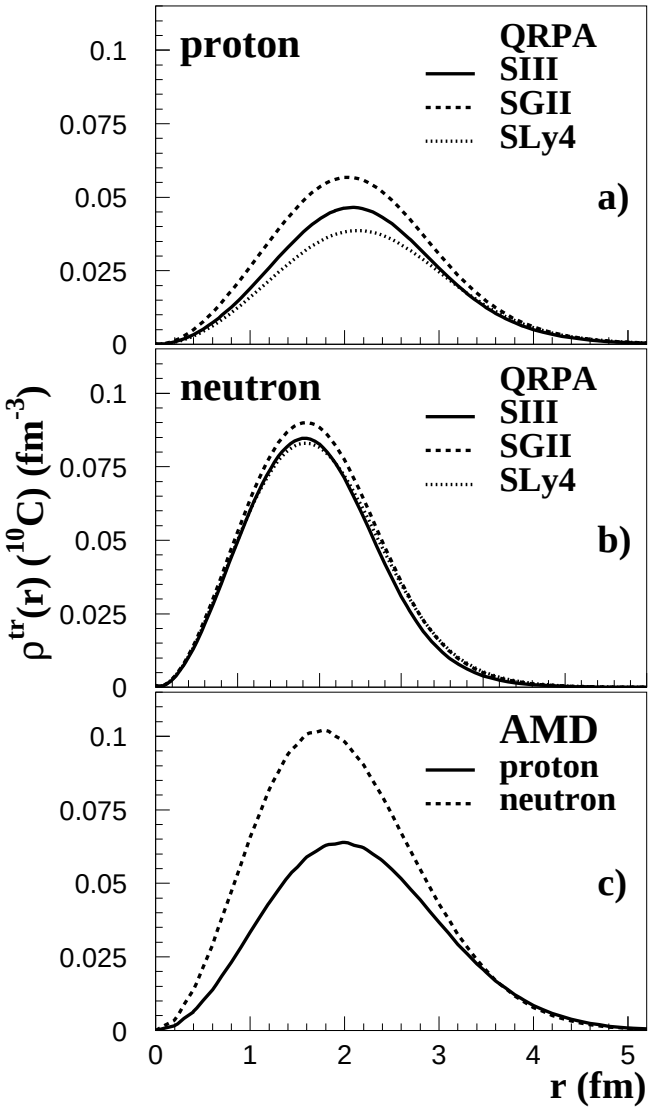

FIG. 15: Neutron and proton AMD and QRPA transition densities from the 0^+_{gs} to the 2^+_1 excited state of ^{10}C.

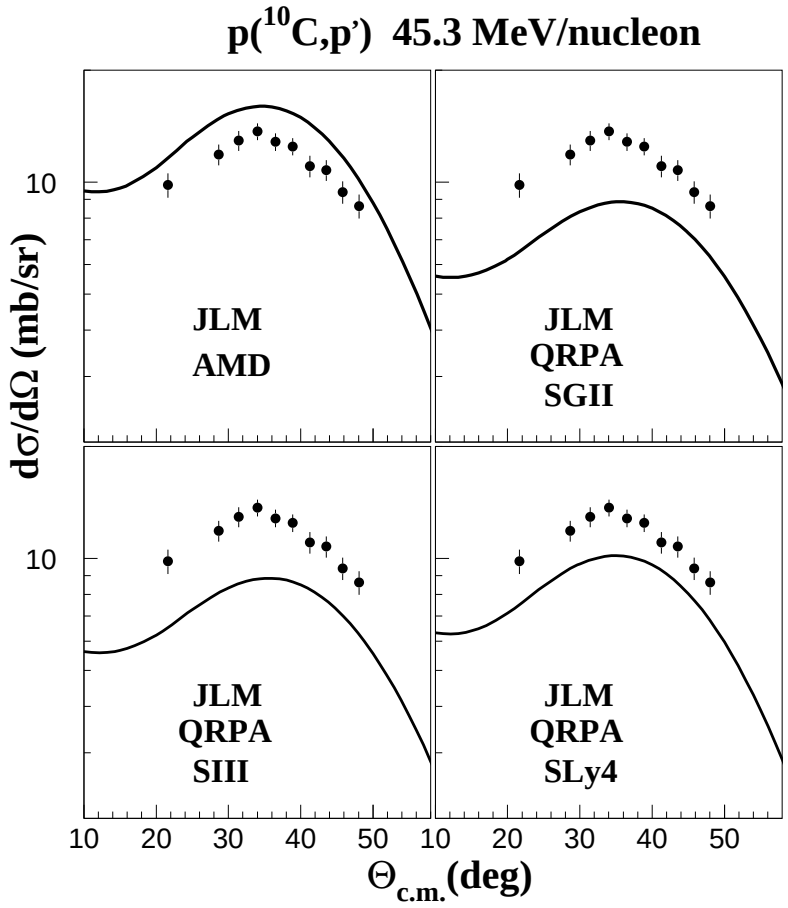

FIG. 16: Inelastic scattering p(^{10}C,p') to the first excited state of ^{10}C (E^* = 3.35 MeV). The experimental angular distribution is compared to the calculations done with the JLM potential using the AMD or QRPA densities (with the three effective Skyrme interactions).

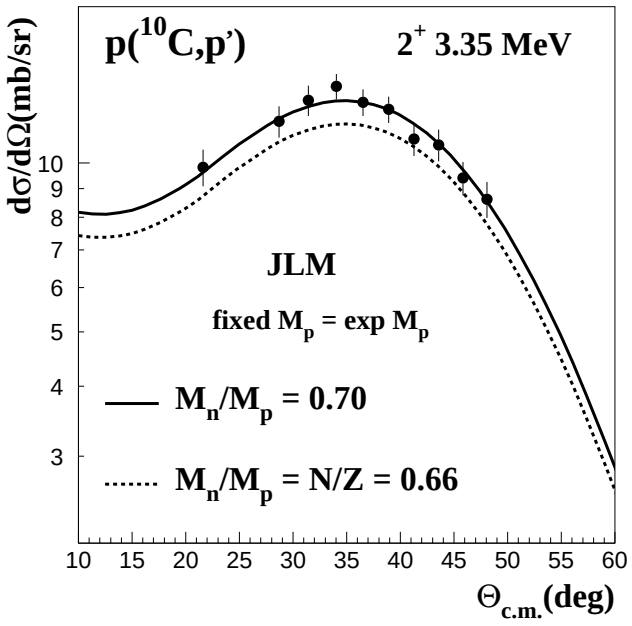

FIG. 17: Inelastic scattering to the first excited state of ^{10}C. The experimental angular distribution is compared to the calculations done with the JLM potential using densities corresponding to the test of different M_n values, as explained in the text.

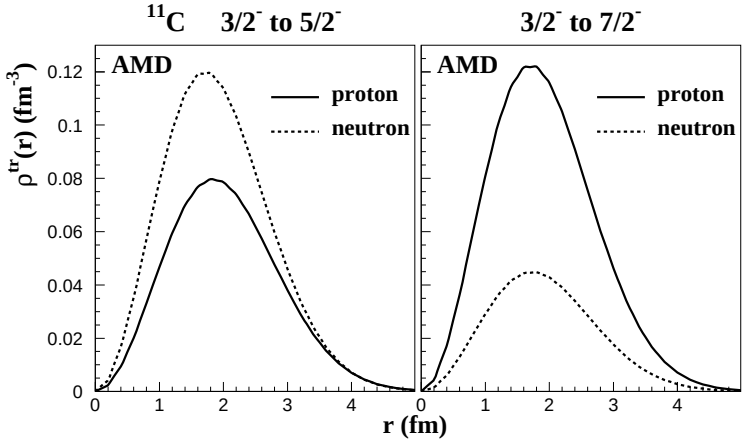

FIG. 18: Neutron and proton AMD transition densities from the $3/2^-$ ground state to the $5/2^-$ (E^*=4.32 MeV) (right) and from the $3/2^-$ ground state to $7/2^-$ (E^*=6.48 MeV) (left) state of ^{11}C.

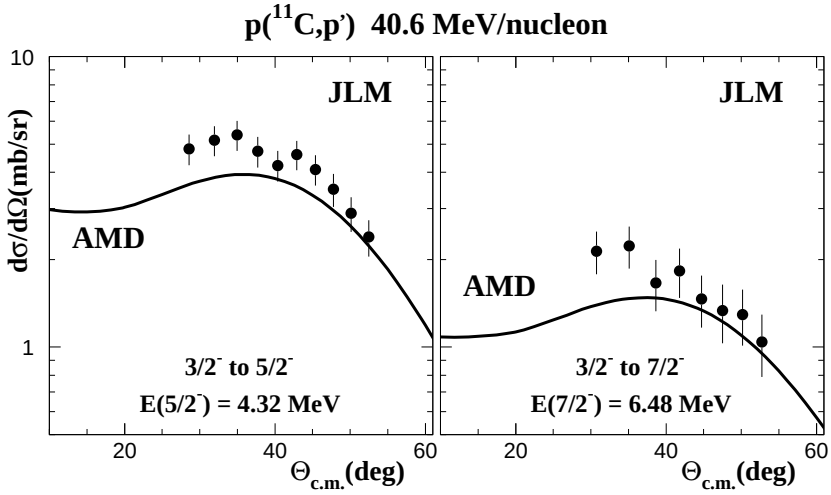

FIG. 19: Inelastic scattering of ^{11}C from the $3/2^-$ ground to the $5/2^-$ state at 4.32 MeV (right panel), and from ground state to the $7/2^-$ state at 6.48 MeV (left) using the AMD densities within the JLM potential.